

Two-dimensional mapping of absolute OH densities in an atmospheric pressure plasma effluent via planar laser-induced fluorescence: effects of He/H₂O and He/O₂ mixtures in N₂ and air, with and without solid targets

María J Herrera Quesada¹ , Sebastian Pfaff² , Jordyn Polito³, Grayson Gall¹ , Mark J Kushner⁴ , Jonathan H Frank² and Katharina Stapelmann^{1,*} 

¹ Department of Nuclear Engineering, North Carolina State University, Raleigh, NC, United States of America

² Combustion Research Facility, Sandia National Laboratories, Livermore, CA, United States of America

³ Department of Chemical Engineering, University of Michigan, Ann Arbor, MI, United States of America

⁴ Department of Electrical Engineering and Computer Science, University of Michigan, Ann Arbor, MI, United States of America

E-mail: kstapel@ncsu.edu

Received 12 December 2024, revised 19 February 2025

Accepted for publication 17 March 2025

Published 26 March 2025



CrossMark

Abstract

Planar laser-induced fluorescence (LIF) was employed to measure the absolute density of hydroxyl radicals (OH) in the effluent of the COST Reference Microplasma Jet for two feed gas mixtures: He/H₂O and He/O₂. Experiments were conducted with the effluent propagating into air and N₂ environments. For the He/H₂O case, measurements were also performed with the effluent impinging on a solid target at varying distances from the jet nozzle. Calibration of the OH-LIF signal from the COST-Jet was achieved by comparing it to a reference signal generated by the photofragmentation of H₂O₂. Results demonstrated that OH densities were sustained longer when the effluent propagates in a nitrogen environment compared to air, particularly with water added to the feed gas. The broader OH distribution in N₂ suggests slower consumption due to the absence of oxygen, which accelerates OH depletion in air via reactions involving O₂ and HO₂. Even when water was not added to the feed, as in the He/O₂ case, appreciable OH densities were observed, due to gas impurities and reactive species interactions with

* Author to whom any correspondence should be addressed.



Original Content from this work may be used under the terms of the [Creative Commons Attribution 4.0 licence](https://creativecommons.org/licenses/by/4.0/). Any further distribution of this work must maintain attribution to the author(s) and the title of the work, journal citation and DOI.

atmospheric humidity, forming reaction fronts that delineate the gas flow. Two-dimensional fluid dynamics simulations elucidated the influence of atmospheric gas entrainment and solid targets on the OH distribution. Experimental trends were further compared with a zero-dimensional chemistry model to explore OH production and consumption mechanisms in air and nitrogen environments.

Supplementary material for this article is available [online](#)

Keywords: atmospheric pressure plasma jet (APPJ), planar laser-induced fluorescence (PLIF), hydroxyl radical (OH), computational fluid dynamics (CFD), plasma chemistry model, plasma effluent surface interaction, absolute calibration

1. Introduction

The hydroxyl radical (OH) is a highly reactive oxygen species (ROS) that plays a crucial role in chemical and biological processes. Its high reactivity is essential in sterilization [1], pollution degradation in water treatment [2], wound healing and oxidative stress-related cancer treatment [3], material surface modification [4], and thin film deposition [5, 6]. Atmospheric pressure plasmas are a valuable source of OH radicals, operating at low gas temperatures and ambient pressure. This allows for a wide range of applications, including treatment of temperature-sensitive materials [1]. However, accurate quantification of OH densities remains a significant challenge because of its high reactivity and transient nature. This is particularly the case for plasma sources where OH is produced in the plasma and transported through an effluent to the surface to be treated, such as the COST Reference Microplasma Jet (COST-Jet [7]), a standard atmospheric pressure remote plasma source.

Several methods have been developed to measure OH densities in gaseous environments, including cavity-ringdown spectroscopy, molecular beam mass spectrometry, and laser-induced fluorescence (LIF). The first two techniques were used by Benedikt *et al* to quantify point-location OH densities in the effluent of a humid feed gas COST-Jet entering a controlled helium atmosphere [8]. Broad-band ultraviolet (UV) absorption spectroscopy was employed by Schröter *et al* to determine OH in the active plasma region of a similar plasma jet device [9]. While these methods are effective for measuring OH densities at discrete locations, they are limited in their ability to capture larger spatial features of OH distributions. Important features in the effluent structure, such as the formation of reaction fronts, and the spatial gradients of OH densities across the plasma effluent, cannot be fully resolved with point-wise measurements. These features are critical for understanding the behavior and transport of reactive species, as well as their propagation into the surrounding atmosphere. Planar LIF (PLIF) is a non-intrusive, highly sensitive imaging technique that provides spatially and temporally resolved measurements of OH distributions [10–12]. A commonly used scheme for OH-LIF measurements involves laser excitation of transitions in the OH ($X \rightarrow A$) band from the ground vibrational state, producing optical emission from transitions in the OH ($A \rightarrow X$)

band that terminate in higher vibrational states of the ground electronic state. The application of LIF for the determination of absolute OH densities has been challenging due to a lack of standardized protocols and calibration methods [10, 11, 13, 14]. Quenching of OH (A) can introduce significant uncertainties even when LIF is used for relative measurements [15]. Absolute OH densities have been determined by integrating experimental results with computational models [16, 17], which also have uncertainties. The development of simpler and standardized protocols for calibrated OH-PLIF measurements would aid in the interpretation of experiments and improve our understanding of the transport of OH radicals.

This paper shows how PLIF can be used to obtain *in-situ* images of the OH density in the effluent of plasma sources. The PLIF signal is calibrated using photofragmentation LIF. In this approach, a pump laser photo-dissociates a precursor molecule, hydrogen peroxide (H_2O_2), to produce a known concentration of OH molecules. A probe laser then excites the OH photofragments, with the resulting PLIF signal providing a reference for calibration. Moreover, vignetting effects, a common issue in near-surface imaging measurements, were corrected by LIF imaging of a fluorescent tracer using the same geometry. This approach enabled accurate probing of near-surface OH densities when the plasma effluent interacted with a solid target.

In this work, OH-PLIF was used to determine absolute densities and spatial distributions of OH in the effluent of the COST-Jet for two gas mixtures, He/ H_2O and He/ O_2 , with the effluent propagating into ambient environments of air and N_2 . For the case of He/ H_2O , measurements were also performed with the effluent impinging on a fused silica disk. Results from computational fluid dynamics (CFD) and global plasma chemistry models were used to aid in the interpretation of the experimental results.

Our results show that once ambient entrainment happens, OH densities are significantly higher and more sustained in a nitrogen atmosphere compared to air, particularly for He/ H_2O where water is directly added to the mixture. The increased spatial reach of OH in N_2 suggests slower consumption due to the absence of oxygen, which accelerates OH depletion in air through enhanced reaction pathways involving O_2 and HO_2 . Even when water is not directly added, as in the case of He/ O_2 , non-negligible amounts of OH are still observed in the

effluent, generated through reactions of reactive species with atmospheric humidity. These interactions form distinct reaction fronts in the region where ambient air is entrained into the effluent. The CFD and zero-dimensional (0D) model capture OH density trends well, accurately reproducing centerline densities and aiding in the identification of key chemical reaction partners. Additionally, the presence of a solid target was shown to expand the lateral distribution of OH, enhancing the availability of this highly reactive species well beyond the core of the effluent.

The paper is organized as follows: section 2 contains the experimental methods. Section 2.1 describes the COST-Jet plasma source and the experimental setup. Sections 2.2 and 2.3 describe the procedure for measuring OH-PLIF in open ambient and with a solid target, as well as the method for absolutely calibrating the results, correspondingly. Section 2.4 provides an overview of the modeling used to explain and contextualize the experimental results: 2D fluid model (section 2.4.1) and 0D plasma chemistry model (section 2.4.2). All results are found in section 3. Section 3.1.1 covers the 2D absolute OH distribution results for a plasma effluent propagating in open ambient, N₂ or air atmospheres, for different initial plasma feed gases: He/H₂O (section 3.1.1) and He/O₂ (section 3.1.2). Each section in 3 also includes discussion related to the corresponding CFD and chemistry model results for each gas admixture utilized. Section 3.2 discusses the results of the 2D absolute OH distribution in the effluent of a He/H₂O plasma when the effluent is approaching a solid target at different distances from the nozzle. Conclusions are presented in section 4.

2. Experimental methods

2.1. Plasma source

The COST-Jet is a capacitively coupled radio frequency excited atmospheric pressure plasma source operating at a frequency of 13.56 MHz and is described in detail in Golda *et al* [7]. The electrodes are 30 mm long, spaced 1 mm apart, and have a width of 1 mm, resulting in an active plasma volume of 30 mm³. Helium was used as the primary feed gas, with small additions of either water vapor (0.25%) or oxygen (0.6%). The total flow rates were: 1 slm for the He/H₂O case and 1.006 slm for He/O₂. High-purity helium and oxygen (Matheson Ultra-High Purity) were used to minimize impurities. To produce the He/H₂O mixture, 108 sccm of dry helium was passed through a water bubbler suspended in a temperature-controlled water bath maintained at 20 °C. Keeping this temperature stable was important for the reproducibility of the measurements, as a small difference in temperature results in variations in the OH densities. The humidified helium was then mixed with 892 sccm of dry helium downstream. Consequently, the resulting 0.25% water mole fraction in the jet was determined based on the vapor pressure of water and the helium flow rates through both the bubbler and the dilution flows. The jet power was held constant at 750 ± 10 mW and was continuously monitored using an oscilloscope connected to the internal current

and voltage probes of the COST-Jet. Measurements were performed in a six-way glass cross with an internal diameter of 5 cm and a leg length of 8 cm and 13 cm in the directions perpendicular and parallel to the laser beam, respectively. The COST-Jet was mounted on the upper port, as shown in figure 1. A translation stage with or without a fused silica disk target was attached to the bottom port. The remaining legs of the cross were sealed by 4.8 mm thick quartz UV fused silica (UVFS) windows for optical access. Enclosing the jet in the glass chamber allowed us to control the environment around the jet, while maintaining atmospheric pressure through outlets at the top and bottom ports. A flow of 8 slm of either air or N₂ (4 slm from each of two axisymmetric top inlets) was supplied into the chamber. The inlets and outlets were positioned sufficiently far from the observed jet effluent that any flow perturbations were negligible and confined to the chamber periphery. House nitrogen, sourced from evaporated liquid nitrogen, was used for the N₂ atmosphere. The air for the atmosphere was supplied by the house air compressor, which may have resulted in slight variations in ambient humidity. Calibration and correction measurements were performed by filling the chamber with uniform concentrations of H₂O₂ vapor or the fluorescent tracers anisole or acetone.

2.2. LIF of OH

PLIF was used to detect OH in the plasma effluent, using the optical setup shown in figure 1. OH molecules were excited by a pulsed laser tuned to the Q₁(1) rotational transition in the A–X (1,0) band at 281.996 nm (referred to as 282 nm) [18], which was continuously monitored with a wavemeter (HighFinesse WS7). This wavelength was produced using a frequency-doubled dye laser at 564 nm (Lambda-Physik Scanmate), pumped by the second harmonic of a 10 Hz Nd:YAG laser (Spectra-Physics GCR-150). The 282 nm laser pulses had an energy of 0.9 mJ and duration of 10 ns. A vertical knife edge was used to crop the laser beams before they entered the six-way glass cross. The beams then passed through the centerline of the COST-Jet's effluent and terminated in a beam dump. This cropping effectively eliminated laser scattering from the jet and/or target and was carefully adjusted to ensure that the measurement area remained unaffected, thereby preserving the accuracy of the laser beam profiles. The resulting fluorescence from the A–X (1,1) and A–X (0,0) bands was detected using an ICCD camera (Andor USB iStar DH312T-18 F-E3) in conjunction with a band pass filter centered at 310 nm ($\Delta\lambda = 10$ nm). The measurements were captured with a 950 ns intensifier gate width.

To obtain quantitative measurements of OH density, the OH-PLIF images were corrected for background, spatial variations in the laser beam profile, optical throughput of the imaging system, and collisional quenching. For background corrections, the light emission from the plasma channel inside the jet along with laser scattering background from the apparatus was recorded and subtracted. Beam profile corrections were performed using two different approaches. In one approach, a portion of the incoming 282 nm laser beam was sampled

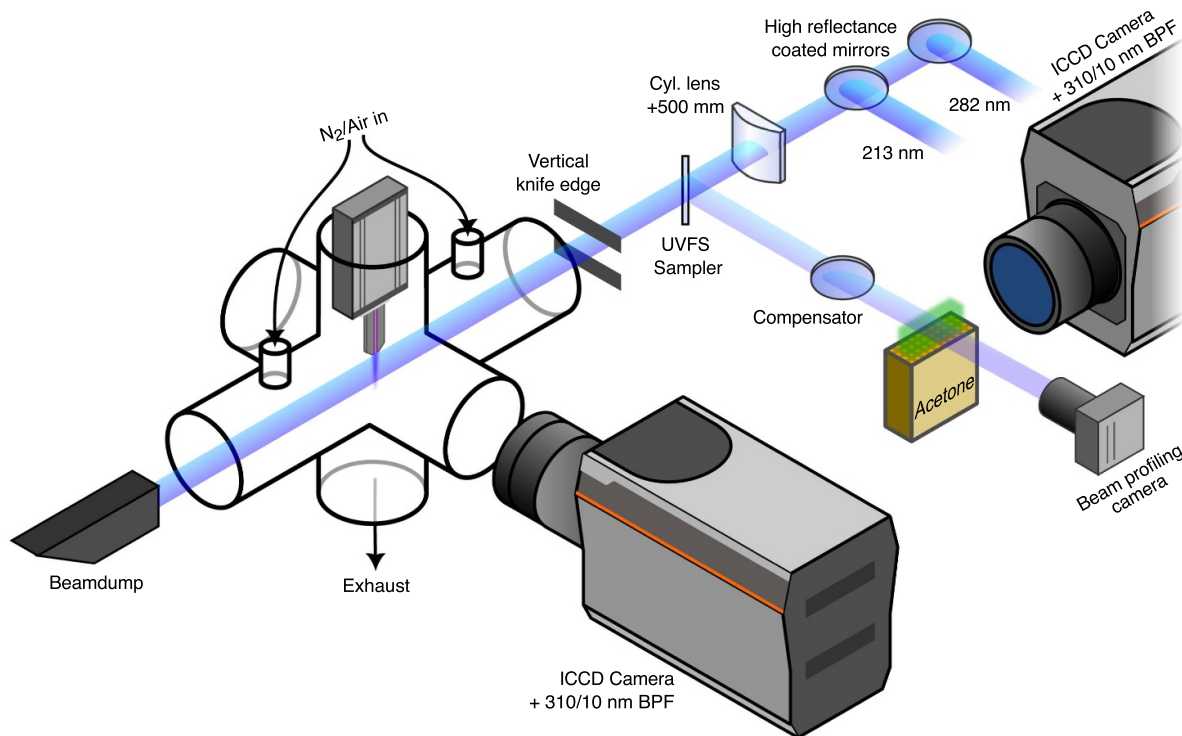


Figure 1. Experimental Setup. The OH-PLIF excitation laser beam (282 nm) is overlapped with the H₂O₂ photodissociation laser beam (213 nm) using high reflectance mirrors. Both beams are formed into sheets using a cylindrical lens (+500 mm). A UV fused silica (UVFS) beamsplitter samples a small fraction of the beams and directs them into a flow of acetone for live beam profiling. The main beams are cropped by a vertical knife edge and enter the six-way glass cross, passing through the centerline of the COST-Jet’s effluent and ending in a beam dump. The ICCD Camera captures the OH-PLIF signal through a 310/10 nm band pass filter.

with a beamsplitter and directed into a flow of argon saturated with acetone vapor. The resulting acetone PLIF signal was recorded using a second ICCD camera that was synchronized with the OH-PLIF measurements. This approach accounted for shot-to-shot fluctuations in the beam profile and energy, but introduced additional complexity in data evaluation, as images from both cameras needed to be matched and intensity differences considered. Alternatively, a separate measurement was performed in which the six-way cross was filled with anisole, a fluorescent tracer with a strong signal produced by excitation at 282 nm [19]. This approach provided measurements of the 282 nm beam profile and vignetting due to obstructions in the PLIF signal collection, such as that of the fused silica disk. These measurements were performed either before or after the OH-PLIF measurements and were implemented when shot-to-shot fluctuations did not need to be monitored. The latter approach greatly simplified the post-processing at the expense of not resolving shot-to-shot fluctuations.

To obtain absolute OH number densities from the LIF signals, spatial variations in collisional quenching rates must be taken into account. The quenching rates are strongly dependent on the local gas composition across the jet effluent because helium is a significantly less efficient quenching partner than water vapor, nitrogen, or oxygen. Thus, there is a large variation in the quenching rates perpendicular to the flow direction as the ambient gas is entrained into the helium-dominated effluent. The density of ambient gases in the effluent increases along the gas flow direction. The OH-PLIF images were

corrected for collisional quenching rates on a pixel-by-pixel basis. The quenching rates were determined in a separate set of measurements that was performed for each jet gas mixture, atmosphere, and geometry (effluent in an open ambient environment or impinging on a target). The temporal decay of the PLIF signal was measured by acquiring a series of PLIF images at ten different delay times between the 282 nm laser pulse and the image intensifier gate. For these measurements, a 5 ns intensifier gate width was used and the intensifier delay time was stepped in 5 ns increments. The resulting temporal decay of the PLIF signal at each location in the image was fit to an exponential function, and the exponential time constant corresponded to the reciprocal of the quenching rate. In cases where the jet effluent impinged on solid targets, a background was recorded for every time step and subtracted from the corresponding OH-PLIF image to account for scattering of the laser beam from the solid surface.

The OH density ([OH]) in the jet effluent, at every pixel, was then given by

$$[\text{OH}]_{\text{jet}} = \frac{S_{\text{jet}}\tau_{\text{ref}}}{S_{\text{ref}}\tau_{\text{jet}}} [\text{OH}]_{\text{ref}}, \quad (1)$$

where the subscripts jet and ref refer to jet and reference mixtures, respectively, S is the PLIF signal intensity, τ is the lifetime of the OH(A)-state, and $[\text{OH}]_{\text{ref}}$ is the OH density in the reference mixture. The corrected PLIF signals in equation 1 are given by $S = (I_{\text{LIF}} - I_{\text{B}})/I_{\text{FF}}$, where I_{LIF} is the intensity

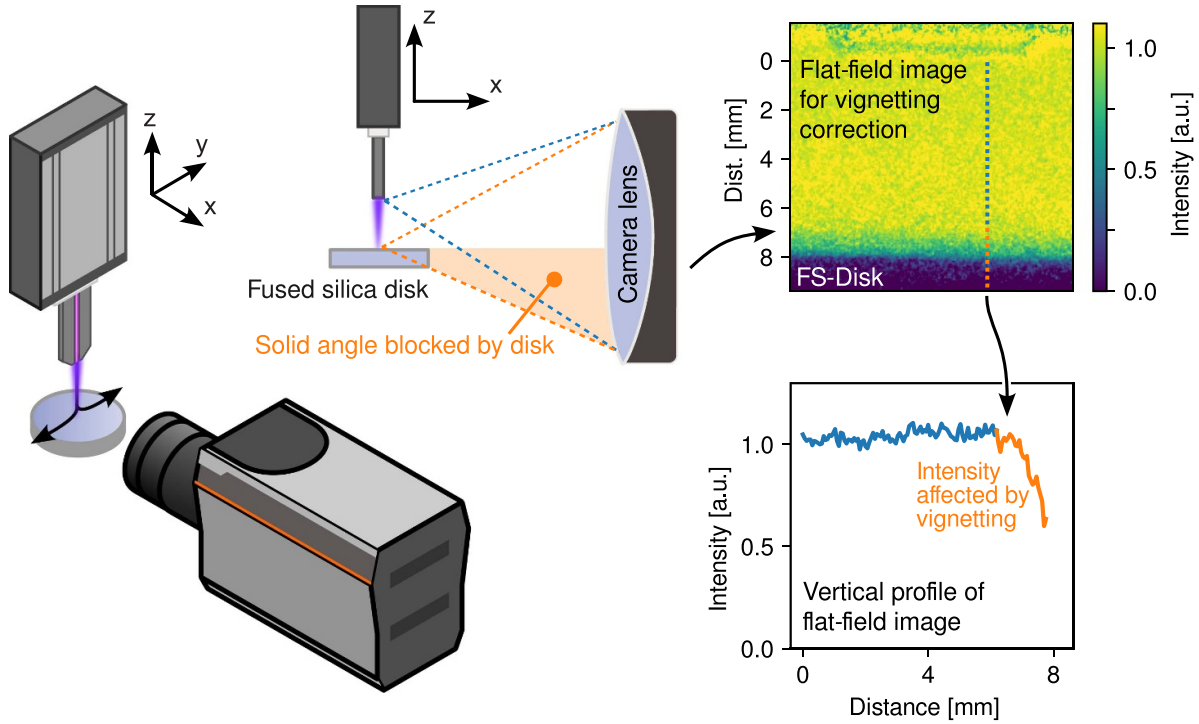


Figure 2. Optical vignetting effects observed during imaging of the jet's effluent impinging on a solid target. The left graphics illustrate the cause of vignetting, while the inset in the upper-right corner shows a flat-field image where signal attenuation occurs near the target surface due to partial obstruction of the optical collection solid angle. The lower panel presents the vertical profile of the flat-field image, demonstrating the signal distribution before applying vignetting corrections.

of the raw PLIF signal, I_B is the background, and I_{FF} is the flat-field correction that accounts for the spatial distribution of the laser beam intensity and the optical throughput of the imaging system. The imaging system throughput includes a correction for vignetting that results in attenuated PLIF signals near the solid targets, which partially obscure the optical collection solid angle. The flat-field corrections were obtained by imaging uniform distributions of the fluorescent tracers acetone and anisole, as described above (see figure 2).

2.3. Absolute calibration of the OH-LIF signal

In order to obtain an absolute calibration of the OH number density, the signal from the COST-Jet was compared with a reference signal $[OH]_{ref}$ generated using the same laser setup to image a known OH number density. This reference OH number density was produced by photodissociation of hydrogen peroxide vapor (H_2O_2) using the 5th harmonic of a Nd:YAG laser at 213 nm. To this end, we changed the atmosphere around the COST-Jet running with the He/ H_2O mixture to an atmosphere containing a small amount of H_2O_2 . This mixture was generated by passing argon through a bubbler filled with 50%wt H_2O_2 in water with the bubbler mounted in a temperature-controlled water bath set to 10 °C. The concentration of the resulting H_2O_2 in the bubbler exhaust gas was determined from an optical absorption measurement by passing the 213 nm laser beam through a 50 cm long absorption cell and measuring the attenuation of the beam. The H_2O_2 in the six-way cross was photodissociated into OH, and the

concentration of the OH photofragments was calculated using

$$[OH] = [H_2O_2] \sigma_{H_2O_2} \Phi_{OH} I_{213} \quad (2)$$

where $\sigma_{H_2O_2}$ is the absorption cross section of H_2O_2 [20], Φ_{OH} is the quantum yield of OH photofragments from photodissociation of H_2O_2 at 213 nm [21], and I_{213} is the 213 nm laser fluence as measured with a power meter (MKS Ophir PE25-C) and a beam profiling camera (DataRay WinCamD-LCM).

The photolytically generated OH was then imaged by the PLIF set-up alongside the COST-jet, which operated with a He/ H_2O admixture, to establish a reference data set used for absolute calibration. The OH number density in the resulting reference was determined to be $[OH]_{ref} = 3 \times 10^{14} \text{ cm}^{-3}$. Differences in OH-PLIF quenching rates between the reference mixture within the jet and the surrounding region containing the photolytically generated OH were measured and accounted for. OH-PLIF measurements for the He/ O_2 admixture were calibrated by comparing the corresponding OH-LIF signal to that of the He/ H_2O reference case.

2.4. Modeling

To aid in the interpretation of the experimental measurements and the consequences of atmospheric entrainment in the effluent gas, a 2D CFD simulation of the flow dynamics was performed. This simulation provided values for the atmospheric entrainment into the effluent centerline, which was then used

Table 1. Properties of the gases used and their respective sources are provided. The diffusion coefficients listed correspond to the interaction of the gases in the leftmost column with helium.

Gas	Diffusion coefficients (cm ² s ⁻¹)	Density (kg m ⁻³)	Viscosity (Pa s × 10 ⁻⁵)
Helium	N/A	0.160 [26]	1.69 [27]
Nitrogen	0.678 [28]	1.126 [29]	1.76 [27]
Oxygen	0.736 [28]	1.283 [30]	2.04 [27]

as input for a 0D chemistry model to investigate the OH production and destruction pathways along the effluent.

2.4.1. 2D fluid model. CFD simulations were performed with the open source Multiphysics Object-Oriented Simulation Environment framework [22], using the finite element Navier–Stokes (NS) module [23]. The finite element mesh used for the calculation was generated using Gmsh, an open source mesh generation tool [24]. A time dependent, weakly compressible model was used [25],

$$\frac{\partial \rho}{\partial t} + \nabla \cdot (\rho \vec{u}) = 0 \quad (3)$$

$$\rho \left(\frac{\partial \vec{u}}{\partial t} + (\vec{u} \cdot \nabla) \vec{u} \right) = -\nabla p + \mu \nabla^2 \vec{u} + \rho \vec{g}. \quad (4)$$

The continuity equation for the concentration of the primary gas, helium, is given by

$$\frac{\partial}{\partial t} (\rho \omega) + \nabla \cdot \rho (\omega \vec{u} - D \nabla \omega) = 0, \quad (5)$$

where D is the diffusion coefficient of helium into air. For a composition of 2 gases, the density, $\rho(\vec{r})$, and viscosity, $\mu(\vec{r})$ were assumed to be a concentration weighted average of the two gas properties,

$$\rho(\vec{r}) = \omega(\vec{r}) \rho_{\text{He}} + (1 - \omega(\vec{r})) \rho_2 \quad (6)$$

$$\mu(\vec{r}) = \omega(\vec{r}) \mu_{\text{He}} + (1 - \omega(\vec{r})) \mu_2 \quad (7)$$

where ω is the mass fraction of helium, ρ_{He} and μ_{He} are the density and viscosity of helium, and ρ_2 and μ_2 are the density and viscosity of the gas in the atmosphere surrounding the COST-Jet. Simulations were run until a steady state in the region of interest was achieved. All gas properties listed in table 1 are at approximately standard temperature and pressure.

The 2D fluid simulations were performed with a helium jet propagating into an air atmosphere, as both the COST-Jet mixtures investigated are at least 99% helium and the difference in diffusion of He was calculated to be less than 0.2% between the air and N₂ atmospheres. To avoid repetition, this simulation will be referred to from here on as the flow field of the COST-Jet into ambient.

2.4.2. 0D plasma chemistry model. *GlobalKin* is a 0D plasma kinetic model that includes the ability to address gas flow using a plug flow approximation, diffusion to surfaces, and changes in gas composition due to heavy particle and electron impact reactions. A detailed description of *GlobalKin* is in [31]. In short, species densities are produced using a continuity equation that includes terms to account for gas flow, heavy particle and electron impact reactions, and diffusion. The gas temperature in the model is determined by solving an energy conservation equation that accounts for joule heating, exothermicity (and endothermicity) of reactions, Franck–Condon heating and thermal conduction to the walls of the reactor. The electron energy equation is solved to provide an average electron temperature.

Electron impact and transport coefficients are obtained from solutions of Boltzmann’s equation for the electron energy distribution over a range of electric-field/gas-density (E/N) values, producing a table of coefficients as a function of average electron energy. The reaction rate coefficients and transport coefficients for the current electron temperature were determined by interpolating the table. Values in the table were periodically updated to reflect changes in the gas composition.

Using a plug-flow approximation, the gas flow was addressed, which is valid for constant-pressure and subsonic-flow systems when diffusion in the flow direction is not important. The gas was tracked down the length of the reactor as a plug of fluid having a cross-sectional area equal to the cross-sectional area of the reactor, where the plug speed is a function of the initial flow rate (in sccm), the gas density, and the cross-sectional area. To maintain constant pressure, the plug speed was adjusted as the gas density changed due to reactions, inflow (entrainment), and changes in gas temperature. Input power (W cm⁻³) was specified as a function of the position in the flow direction when using the plug flow approximation. The power density profile was normalized so that the integral of the power density throughout the reactor profile was equal to the total desired input power. Power along the reactor axis was constant, except for a 1 mm ramp-up distance at the top of the reactor and a 1 mm ramp-down distance at the reactor outlet. The power was not dissipated beyond the limits of the electrodes.

The reaction mechanism included 101 gas-phase species and 2183 gas-phase reactions. Gas-phase species include He, O₂, N₂, and H₂O, as well as their relevant ions and electronically and vibrationally excited species. A detailed description of the gas-phase mechanism is provided in [31, 32]. Any deviations in reaction rate coefficients from these models are presented in Supplemental table 1. The simulated domain was meant to approximate the COST-jet. Plasma with the same gas composition as the experiment was generated with a rectangular cross-sectional area of 1 mm × 1 mm and a total gas inlet flow rate of 1 slm. The gas plug traveled along the 30 mm reactor length, where depending on conditions, the gas temperature increases by about 50 K flowing through the plasma before exiting the powered region and coming into contact with ambient humid air or nitrogen atmosphere. Ambient gas was injected into the plug flow upon exiting the reactor to

approximate the interdiffusion of the He effluent with the ambient. At this stage, the gas temperature in the plume rapidly decreases due to thermal conduction and the inflow of colder ambient gas. The amount of injection was chosen to match the mole fractions predicted by the CFD calculations. *GlobalKin* was used to model OH densities for the two experimentally investigated gas mixtures (He/H₂O and He/O₂), propagating into air and nitrogen atmospheres. The air and N₂ atmospheres are simulated with initial mole fractions of N₂/O₂/H₂O = 0.78/0.20/0.02 and N₂/H₂O = 0.98/0.02 [33].

3. Measurements of OH densities

3.1. Plasma effluent flow into open ambient

3.1.1. He/H₂O. For the flow of He/H₂O into the open ambient, an OH density of $3 \times 10^{14} \text{ cm}^{-3}$ was measured at the exit of the jet nozzle in both air and N₂ atmospheres, as shown in figures 3(a) and (b). The 2D computed flow field of He effluent into ambient is shown in figure 3(c). As soon as the effluent starts to mix with the surrounding atmosphere, pronounced differences are observed in the OH densities between air and N₂ atmospheres. In air figure 3(a), the density of OH decays rapidly, while in the N₂ atmosphere figure 3(b) OH can still be detected after 30 mm from the nozzle exit.

The horizontal expansion of the effluent also differs between air and N₂ atmospheres. In air, OH is more confined to the center region of the effluent with the OH density tapering to below detection limits at 30 mm. The density of OH also tapers in the axial direction in N₂, though at a rate that is about half that in the air ambient.

The He flow field in figure 3(c), shows the extent to which the inert helium carrier gas is expected to expand in the horizontal and vertical directions. Comparing the He flow field to the measured OH distributions demonstrates that OH propagation is limited by chemical reactions. In N₂ atmosphere (figure 3(b)) the propagation of OH shows a similar shape to the propagation of He (figure 3(c)) but does not reach the same extent in vertical and horizontal direction. The differences are more pronounced when the effluent is propagating into air (figure 3(a)), where the OH density shows a significant decline in both the vertical and horizontal directions, indicating that chemical reactions with oxygen in air reduce the OH density rapidly. A chemical pathway analysis is provided at the end of this section.

OH densities along the central axis as a function of distance from the jet nozzle are shown in figure 4 for air and N₂ ambient. The ambient gas entrainment extracted from the 2D fluid simulations is also shown. For the first 4 mm from the nozzle exit, the density of OH on the center line is nearly identical for the air and N₂ atmospheres. The OH density decreases linearly until 4 mm from the nozzle, at which point the densities in the different atmospheres begin to diverge. The CFD simulation shows that the entrained ambient gas entrainment does not reach the center axis until 4 mm from the nozzle. These results suggest that the divergence of the centerline OH densities between the N₂ and the air atmospheres is due to the ambient gases reaching the axis of the effluent. The linear decrease

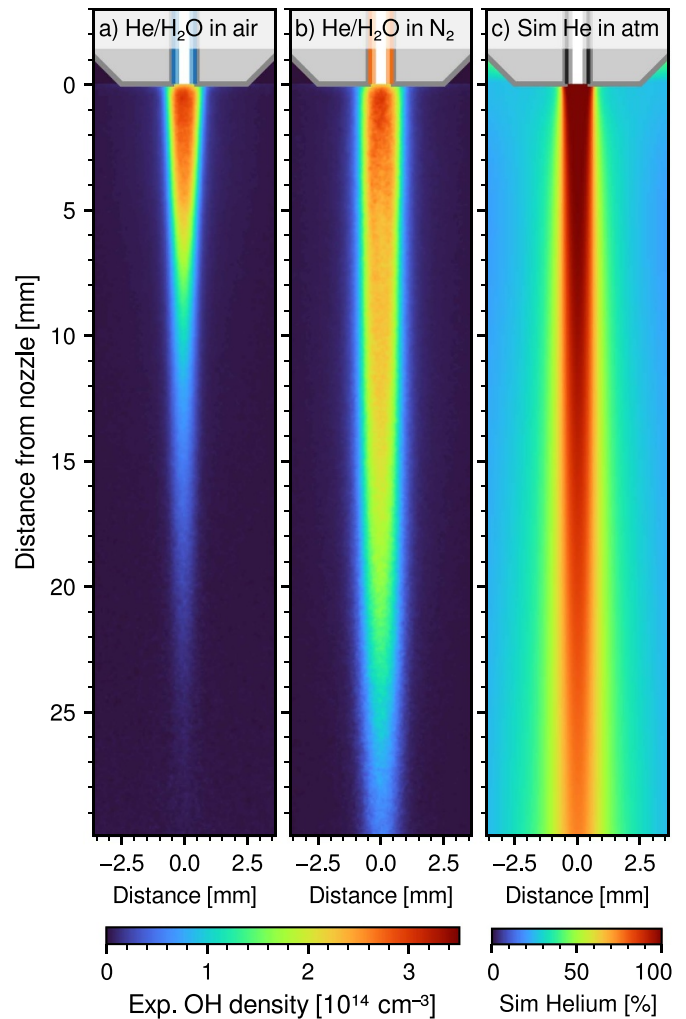


Figure 3. OH density measurements for the open effluent of a He/H₂O COST-Jet plasma in (a) air and (b) N₂ atmosphere. (c) 2D computed flow field of the helium percent of the COST-Jet (without plasma) into ambient.

in OH density observed before 4 mm for both atmospheres is likely due to chemical reactions and not due to interactions with the surrounding atmosphere.

Beyond 4 mm, the OH density in the N₂ atmosphere is relatively constant until 10 mm. Beyond 10 mm from the nozzle, the OH density decreases nearly linearly with distance. Between 4 and 10 mm, any consumption of OH is balanced with production of OH in reactions with the surrounding (humid) nitrogen. These conditions correspond to an ambient gas entrainment of <5%. The OH density in the effluent expanding into air decreases exponentially beyond the 4 mm divergence point until the end of our imaging region as OH is consumed in reactions with the entrained air.

To better quantify the differences between the OH propagation in the two atmospheres, horizontal profiles of OH density are shown in figure 5 for the He/H₂O mixture flowing into open ambient air and N₂ atmosphere. Densities are presented for nozzle distances from 0 mm to 16 mm. The profiles reveal the significant differences in the behavior of OH radicals between the two atmospheres. In N₂, the OH density remains more

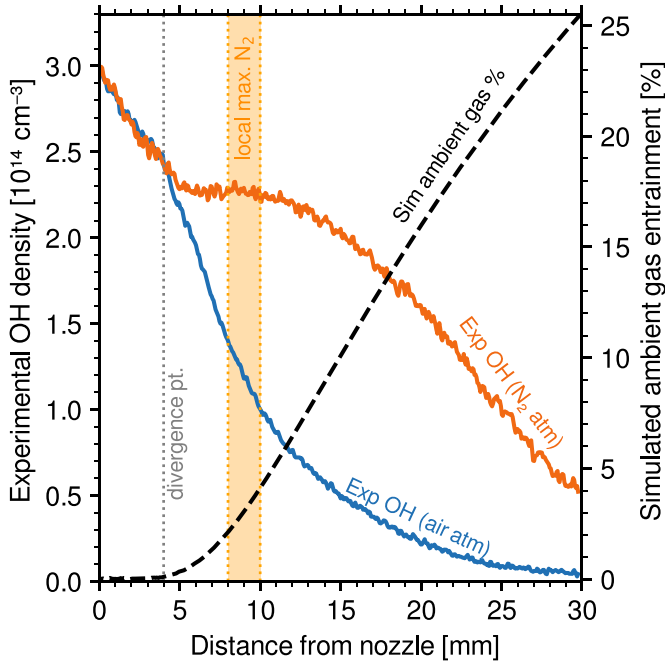


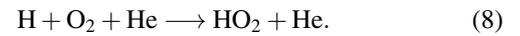
Figure 4. Measured centerline OH density profiles in open effluent of a He/H₂O COST-Jet plasma, in air (blue) or N₂ (orange) atmosphere, corresponding to data in figures 3(a) and (b). The black dashed line corresponds to the centerline percent of ambient gas entrainment from the CFD simulation seen in figure 3(c). Divergence point at 4 mm indicates the location where the evolution of the centerline OH number density deviates for the different atmospheres, while the local maximum, identifying a slower OH decay in N₂, is marked as a range from 8 to 10 mm.

sustained across a broader horizontal extent, while in air, the density decreases rapidly both vertically and horizontally. At 16 mm distance from the nozzle, the peak OH density in N₂ reaches approximately $2 \times 10^{14} \text{ cm}^{-3}$, with densities above $0.5 \times 10^{14} \text{ cm}^{-3}$ still present 1 mm from the center axis. In contrast, the peak OH density in air is five times lower than in N₂ at this distance, reflecting the rapid consumption of OH radicals due to reactions with O₂.

These trends highlight the significant influence of the ambient atmosphere on the spatial distribution of OH radicals. The broader, sustained OH profile in N₂ suggests a slower consumption rate, allowing the radicals to persist farther from the plasma core. In air, however, the presence of oxygen leads to enhanced chemical reactions that quickly deplete OH, resulting in a more restricted spatial profile.

Results from the global 0D model for OH densities are presented in figure 6, for the He/H₂O plasma effluent flowing into humid N₂ or air. This chemistry model incorporates ambient gas injections to match the percentage of entrained ambient gas along the jet’s central axis, as determined by the CFD simulations. These results enable a direct comparison with the PLIF-derived OH densities seen in figure 4. The OH densities produced in the model match the experimental trends for both atmospheres, considering the limitations of the 0D plug-flow model. At the exit of the plasma channel, the model predicted an OH density of $3.7 \times 10^{14} \text{ cm}^{-3}$ for both atmospheres, while

the experimental measurement is $3 \times 10^{14} \text{ cm}^{-3}$. The initial 4 mm shows that the decay of OH is independent of the ambient gas, as observed in the experiment. Beyond 7 mm, the predicted OH densities remain higher in the N₂ atmosphere than in the air atmosphere, as observed experimentally. The exponential decay in OH densities for the air atmosphere as a function of distance from the nozzle beyond 4 mm is in good agreement with the experiment. However, the predicted OH densities increase upon ambient injection for the air atmosphere. The resulting peak at around 5 mm is a clear discrepancy with the experiment and is attributed to a spike in HO₂ production near the reactor outlet. This occurs due to the following three-body reaction of H with O₂ and He, where the rate of formation is constrained by the availability of O₂, while H atoms-abundant due to H₂O dissociation-further drive the reaction,



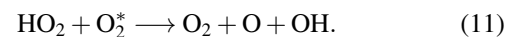
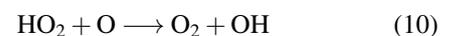
This peak is an artifact of the manner in which ambient air is impulsively injected into the plug flow ‘effluent’ while also being instructive on the production of OH. A portion of this increase in production may be due to an overestimation of the three-body rate coefficient used for these reactions. Most of the reaction rate coefficients for three-body reactions involving O, OH, H, HO₂, and H₂O₂ were estimated using values for N₂ acting as the third body [34, 35], as detailed in SI table 1. It is likely that the rate coefficient with He as the third body is smaller as He is less likely to stabilize the intermediate transition state. A smaller rate coefficient would reduce the formation of HO₂.

Three regions are shown in figure 6, defined to facilitate the chemistry analysis based on ambient gas entrainment: Region I, 0–4 mm, represents the zone of no ambient gas entrainment (0%), Region II, 4–15 mm, encompasses moderate ambient gas entrainment (<10%), and Region III, 15–30 mm, captures the area of high ambient gas entrainment (<25%). The average production and consumption reactions of OH in these three regions are shown in figure 7. Since overall rates are important, each region also has the total rate of OH production or consumption.

In Regions I and II, OH is produced predominantly by (figure 7(a))



irrespective of whether there is entrainment of air or N₂. In contrast, for high entrainment (Region III), switching from N₂ to air shifts the dominant production pathways to reactions (10) and (11), with (11) playing the most significant role. In reaction 11, O₂^{*} refers to both electronically excited states O₂(¹Δ_g) and O₂(¹Σ_g⁺), where is O₂(¹Δ_g) typically present at densities several orders of magnitude higher than O₂(¹Σ_g⁺),



In the nitrogen atmosphere, reaction (9) is consistently the dominant pathway for OH production throughout the distance,

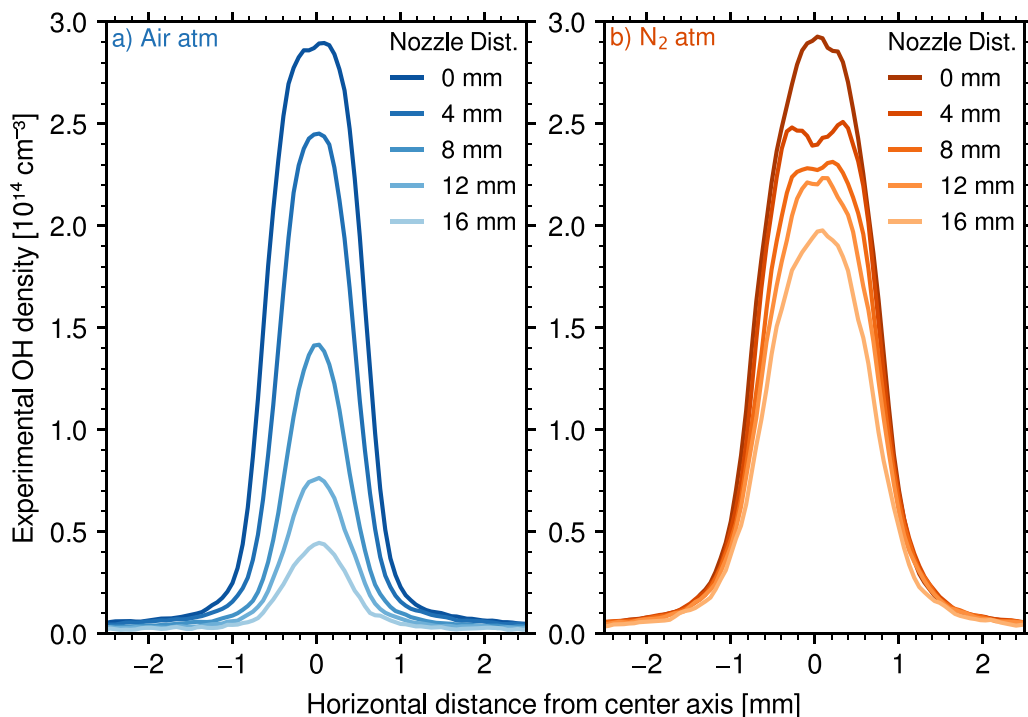


Figure 5. Horizontal profiles of measured OH density, corresponding to the OH PLIF image from the He/H₂O open effluent in (a) air and (b) N₂ atmospheres, as seen in figures 3(a) and (b), with varying distance from the COST-Jet's nozzle.

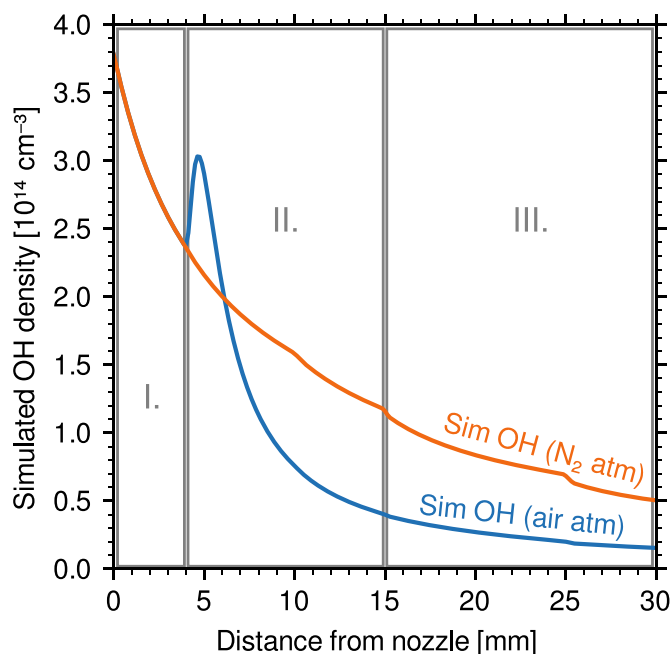


Figure 6. Predicted OH density along the effluent centerline from the chemistry simulation of the He/H₂O COST-jet in air and N₂ atmospheres. Regions are defined based on the CFD model to emphasize variations in ambient gas entrainment and facilitate the chemistry analysis: Region I (0–4 mm) represents the zone of no ambient gas entrainment (0%), Region II (4–15 mm) includes moderate ambient gas entrainment (<10%), and Region III (15–30 mm) indicates high ambient gas entrainment (<25%).

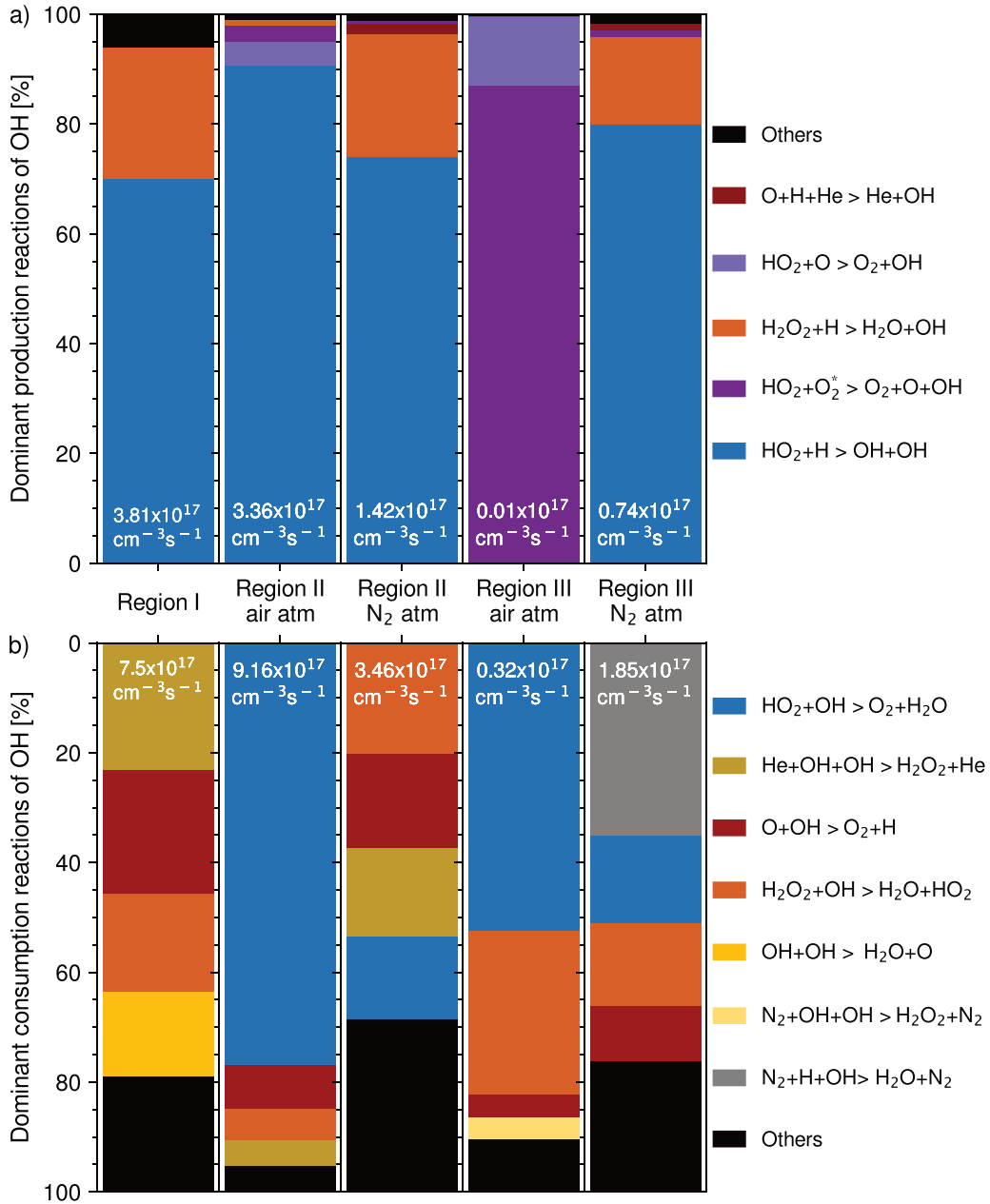
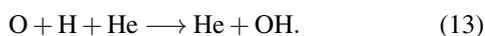
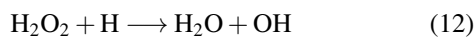


Figure 7. Dominant production and consumption reactions of OH derived from the chemistry simulation of the He/H₂O COST-jet effluent in air and N₂ atmospheres. The primary (a) production and (b) consumption reactions of OH are plotted as percentages across Regions I (0% ambient gas entrainment), II (<10% ambient gas entrainment), and III (<25% ambient gas entrainment), as defined in figure 6. For clarity, reactions are color-coded as follows: HO₂ reactions in blue, O-species reactions in red, combined HO₂ and O-species in purple, H₂O₂ in orange, OH recombination in yellow, three-body reactions (not covered above) in gray, and other reactions in black. The total rates of OH production and consumption are indicated in each region.

while reactions (12) and (13) are the next highest contributors,



HO₂ clearly plays a dominant role in the production of OH in both atmospheres for this He/H₂O plasma effluent, as it is a reactant in three out of the top five reactions for OH production.

Although the model likely over predicts the density of HO₂ at 5 mm in the air atmosphere, the fact that the dominant production mechanism is the same in the nitrogen atmosphere gives credence to the suggested production mechanism. For the He/H₂O mixtures flowing into air or N₂ ambient, the model predicts that the density of HO₂ at the outlet of the COST-Jet nozzle, before mixing with the ambient, is about 1% that of OH for both ambients ($3 \times 10^{12} \text{ cm}^{-3}$). Since the three-body reaction (reaction (8)) contributes the most to HO₂ production in the region where the effluent comes into contact with the atmosphere, its formation is strongly influenced by O₂

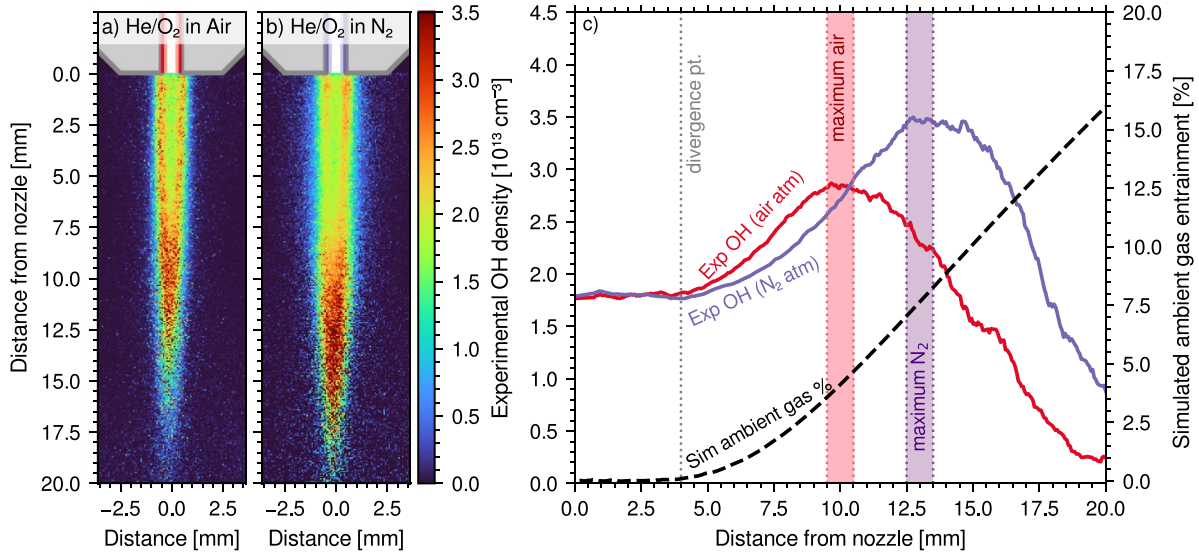
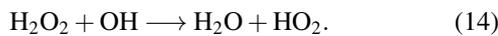


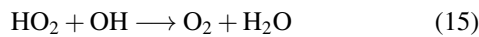
Figure 8. OH number density measurements for the open effluent of a He/O₂ COST-Jet plasma in (a) air and (b) N₂ atmospheres. (c) The centerline profiles of measured OH density, as a function of distance from the jet nozzle along with the centerline profile of the ambient entrainment percent from the 2D fluid dynamics simulation. Divergence point at 4 mm indicates the location where the evolution of the centerline OH number density deviates for the different atmospheres. Additionally, the location of the maximum OH density for each atmosphere is marked.

availability. When flowing into an N₂ ambient, there is only a slight increase in HO₂ density, as the O₂ concentration remains low. In contrast, when flowing into an air ambient, the presence of O₂ leads to a rapid increase in HO₂ density, which in turn rapidly consumes the H atoms produced in the plasma. In Region II, this is also reflected in the total rate of OH production being 2.4 times higher in air ($3.4 \times 10^{17} \text{ cm}^{-3} \text{ s}^{-1}$) than in N₂ ($1.4 \times 10^{17} \text{ cm}^{-3} \text{ s}^{-1}$) when reaction (8) dominates the production mechanism.

It would then follow that reactions with HO₂ that form OH (reactions (9), (10), (11)) are more important for He/H₂O plasma effluent in ambient air than in N₂ atmosphere. In the N₂ atmosphere, HO₂ is formed by reaction (8) from O₂ that is formed as a by-product from reactions of H₂O dissociation products and by reaction (14),



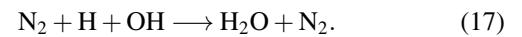
HO₂ again comes into play in the air atmosphere (Regions II and III), but for the consumption of OH following reactions (15) and (16), as O₂ ultimately produces more HO₂,



In Region II with air, the OH consumption rate is 2.7 times greater than its production rate, whereas in Region II with N₂, the consumption rate is only 2.4 times larger. Since the experimentally observed OH density results from the balance between production and consumption rates, these findings explain why OH consumption occurs more slowly in the N₂ atmosphere compared to the O₂-containing air environment, where HO₂ is produced as described by equation (8).

While the overall role of atomic hydrogen is less significant for OH consumption than for production, H becomes the

dominant reaction partner for OH in the high air entrainment region (Region III) by reaction (17),



The production and consumption mechanisms for He/H₂O mixtures are dominated by the interactions of HO₂, H₂O₂, and atomic oxygen. The trends suggest that if the goal is to deliver OH through the effluent of a plasma jet to a surface, isolating the effluent from ambient oxygen would be best. This could be accomplished with an N₂ co-flow around the jet.

3.1.2. He/O₂. LIF measurements were made in the effluent of a He/O₂ jet mixture, consisting of 6 sccm of pure O₂ added to 1 slm of He. Although no water is added to the feed gases there are water impurities in the gas provided by the manufacturer, which results in the detection of OH in otherwise pure helium discharges [8, 36, 37]. For example, 99.999% pure He from a major gas supplier has several ppm of H₂O, which at atmospheric pressure corresponds to a density of about $5 \times 10^{13} \text{ cm}^{-3}$ or a few mTorr. Despite the challenge of eliminating impurities, even with high-purity gases, these results offer a guide for estimating OH production from impurities in this commonly used plasma admixture.

The 2D OH density measurements in the COST-jet effluent in air and N₂ atmospheres are shown in figure 8. The OH density at the nozzle's exit for both atmospheres is approximately $1.8 \times 10^{13} \text{ cm}^{-3}$ indicating the water impurity is largely dissociated. Overall, OH densities are lower than in the He/H₂O mixture, to the point that the OH fell below the detection limit about 20 mm from the nozzle. The spatial distributions of OH in the N₂ and air atmospheres exhibit a greater similarity to each other than their counterparts in the He/H₂O case. For

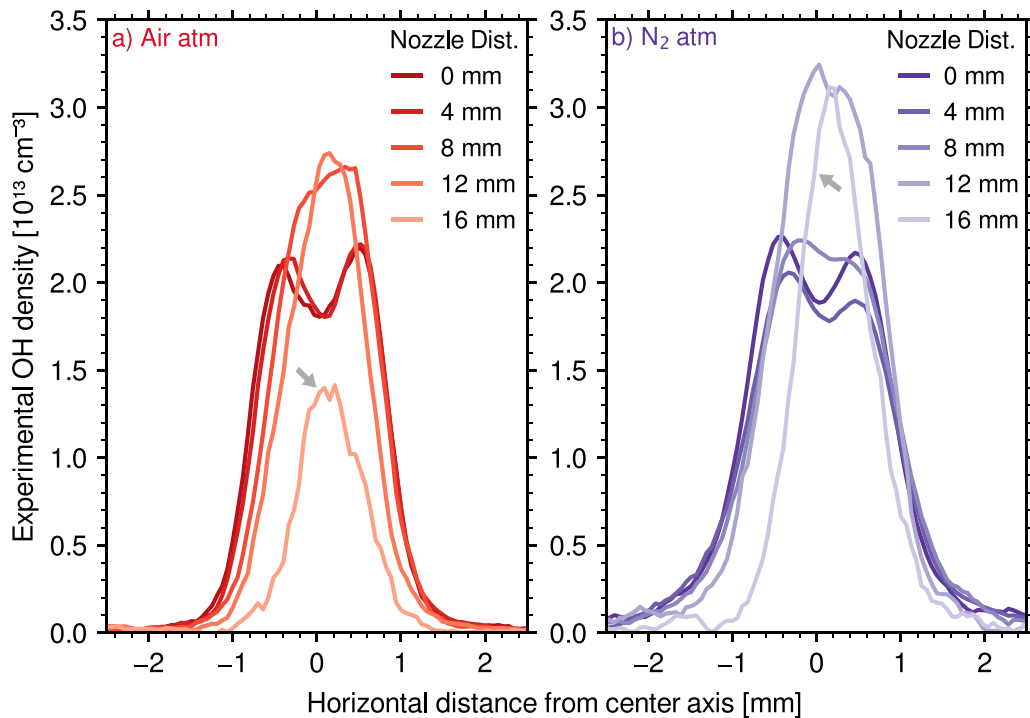


Figure 9. Horizontal profiles of measured OH density, corresponding to the OH PLIF image from He/O₂ open effluent in air and N₂ atmospheres, as seen in figures 8(a) and (b), with varying distance from the COST-Jet nozzle. The depicted arrows point to the farthest downstream profile at 16 mm from the nozzle, where the trend of increasing OH with distance from nozzle has already inverted.

the He/H₂O case, the main difference between the two atmospheres is that the OH extends about 4 mm longer than into the air atmosphere. The largest OH densities at the nozzle exit are adjacent to the electrodes, where sheath heating in the plasma produces electron impact dissociation of H₂O impurities and dissociative excitation transfer occurs from excited He to H₂O. The OH density distribution then converges towards the axis, with the maximum OH density occurring on-axis 10–15 mm from the nozzle. Notably, the OH production forms ‘reaction fronts’ at the periphery of the jet’s effluent that converge towards the axis as ambient gases diffuse into the jet. The formation of these fronts indicate that OH is generated where plasma reactive species interact with ambient humidity rather than solely depending on impurities in the gas admixture. These trends suggest that gas dynamics and atmospheric humidity (common to both atmospheres) dominate OH production, consumption, and redistribution.

The axial OH densities for both atmospheres are plotted as a function of distance from the jet nozzle in figure 8(c). The ambient gas entrainment percents obtained from the CFD simulations are also shown. As also observed in the He/H₂O case (figure 4) the OH densities are similar for both atmospheres until 4 mm from the nozzle. Unlike the He/H₂O case, the OH density remains fairly constant for this region without atmospheric entrainment. After 4 mm, the OH densities increase in both atmospheres. This increase can be attributed to the reaction fronts converging toward the center of the effluent as the horizontal width of the OH density distribution decreases.

The axial OH density in the air atmosphere has a maximum of $2.85 \times 10^{13} \text{ cm}^{-3}$ around 9.5–10.5 mm from the nozzle. In the N₂ atmosphere, the maximum density is $3.5 \times 10^{13} \text{ cm}^{-3}$ around 12.5–13.5 mm from the nozzle. The maxima in OH densities occur when the ambient entrainment is 4% for the air atmosphere and 8% for the N₂ atmosphere. With the fluid dynamics and ambient humidity being similar, reactions with O₂ in the air ambient results in a net reduction in OH density.

Figure 9 compares the horizontal profiles of measured OH density for He/O₂ in air and N₂ atmospheres, illustrating how OH evolves with increasing distance from the COST-Jet nozzle. As expected, compared to figure 5 the profiles exhibit a noticeable increase in noise due to lower overall OH densities. The horizontal reach of OH extends similarly in both atmospheres; however, a slightly broader spread and higher densities are observed in the N₂ atmosphere. At 16 mm from the nozzle, indicated by the arrows, the profiles invert, showing a decrease in OH density and reflecting shifts in entrainment dynamics.

The densities of OH predicted by the global chemistry model for the He/O₂ plasma effluent flowing into humid N₂ and air atmospheres are shown in figure 10. For this simulation, a water impurity was added to the inlet gas so that the predicted OH density at the exit of the nozzle approximated that of the experiments. The OH density at the nozzle in the simulation was $1.35 \times 10^{13} \text{ cm}^{-3}$ and was produced by adding 8 ppm of water to the simulated feed gas, which is comparable to estimated impurities in the literature [8, 38]. Similar to the

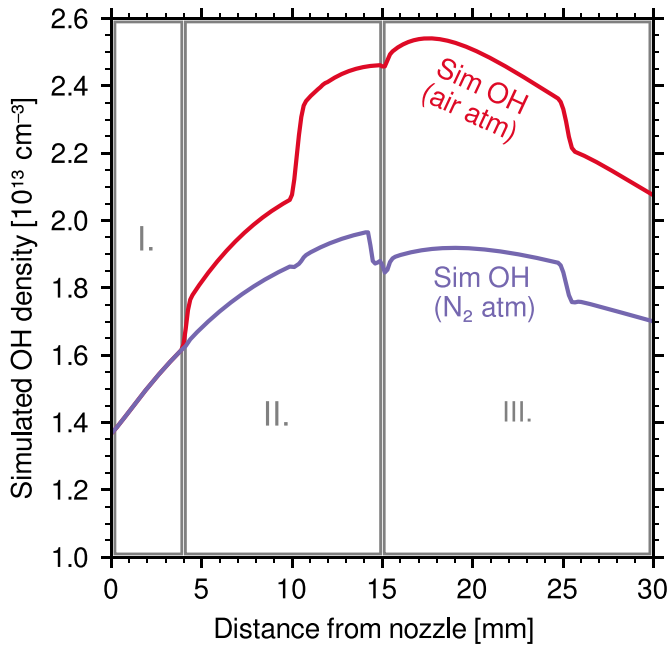


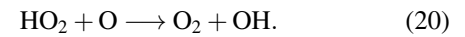
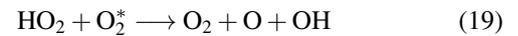
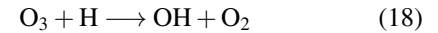
Figure 10. Predicted OH density along the effluent centerline from the chemistry simulation of the He/O₂ COST-jet in air and N₂ atmospheres. Regions are defined based on the CFD model to emphasize variations in ambient gas entrainment and facilitate the chemistry analysis: Region I (0–4 mm) represents the zone of no ambient gas entrainment (0%), Region II (4–15 mm) includes moderate ambient gas entrainment (<10%), and Region III (15–30 mm) indicates high ambient gas entrainment (<25%).

He/H₂O chemistry simulation, ambient gas entrainment into the effluent was achieved by discrete injections at rates aligned with CFD simulations. This approach accounts for the step-wise changes observed in the predicted OH densities, reflecting variations in ambient gas incorporation.

These discrete changes reflect the sensitivity of the OH densities to atmospheric entrainment, regardless of the atmosphere type. The trends from the model agree with those of the experiments. As before, the areas of interest are: Region I, 0–4 mm, representing the zone without ambient gas entrainment (0%), Region II, 4–15 mm, encompassing moderate ambient gas entrainment (<10%), and Region III, 15–30 mm, area of high ambient gas entrainment (<25%). In Regions I and II, the OH density increases with distance from the nozzle and the ambient entrainment in Region II alters the rate of increase, most notably for the air atmospheres. In Region III, ambient entrainment decreases the OH density. As the OH is mainly created due to mixing with the ambient, the model is sensitive to humidity levels in the surrounding atmosphere. With the global model being volume averaged, the experimentally observed ‘reaction fronts’ are not resolved.

The dominant reactions contributing to OH production and consumption in Regions I, II, and III are shown in figure 11(a) and (b), respectively. The percentage contribution of each region is an average over each region. The mechanisms for the production and consumption of OH are not very sensitive to the composition of the atmosphere (air or N₂) with which the effluent mixes, as observed in the experiments.

In both atmospheres, the dominant reactions for OH production are:

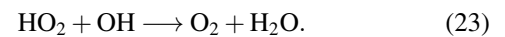
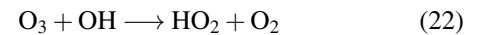


In Regions I and II (no to medium entrainment), ozone plays a major role in the production of OH via reaction (18), even though this gas mixture only contains 0.6% oxygen. As atmospheric entrainment increases (Region III), the main production of OH switches to reactions with HO₂, as more humidity from the atmospheres is added to the effluent. A single reaction dominates the consumption of OH regardless of the atmosphere or position in the effluent:



As the reaction partner O is mainly produced in the active plasma from electron impact dissociation of O₂ and dissociative excitation transfer from He*, the consumption of OH in both atmospheres is similar.

As observed in figure 9, the experimental results indicate a broader horizontal spread of OH in the N₂ atmosphere and a longer axial extension in the effluent. This suggests that the presence of O₂ in the surrounding atmosphere significantly influences OH consumption. As air increasingly mixes with the effluent, additional OH consumption reactions become prominent, particularly within Region III, such as:



As more oxygen mixes with the effluent and additional O-atoms are produced, O-atoms can either react with OH (Reaction (21)) to consume OH or combine with O₂ to form O₃, which then in turn can also consume OH (Reaction (22)). To a lesser extent HO₂ is produced when more oxygen and humidity enter the effluent, providing another pathway for OH consumption that is less likely to occur in the N₂ atmosphere.

3.2. Plasma effluent onto solid targets

Atmospheric plasma jets are frequently applied to treat surfaces—such as cells, skin, or water—using reactive species carried within the effluent. To enhance our understanding of these interactions and optimize OH flux in plasma treatments, PLIF measurements of OH densities were performed for COST-jet effluents impinging on solid targets. Specifically, OH distributions were measured for the He/H₂O mixture flowing into air and N₂ ambients, with solid targets positioned at 4 and 8 mm from the nozzle exit, as shown in figure 12. The 4 mm distance was selected based on extensive prior research conducted at this gap distance [36, 37, 39–43], providing valuable context for those studies. As shown in this paper, this distance also marks the point where atmospheric gas entrainment begins along the effluent centerline, making it critical for examining target influence. The 8 mm distance was chosen as

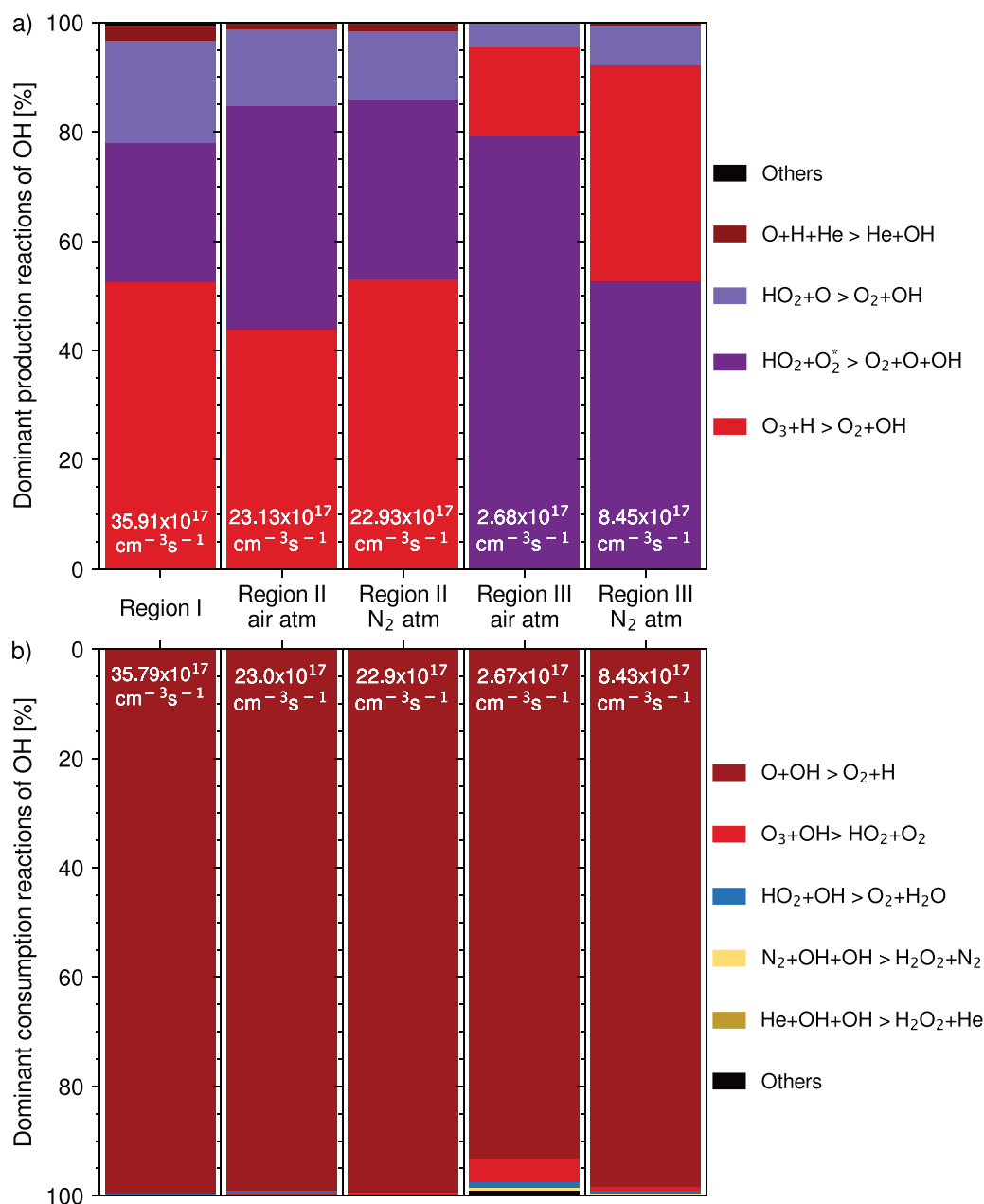


Figure 11. Dominant production and consumption reactions of OH derived from the chemistry simulation of the He/O₂ COST-jet effluent in air and N₂ atmospheres. The primary (a) production and (b) consumption reactions of OH are plotted as percentages across Regions I (0% ambient gas entrainment), II (<10% ambient gas entrainment), and III (<25% ambient gas entrainment), as defined in figures 10 and 6. For clarity, reactions are color-coded as follows: HO₂ reactions in blue, O-species reactions in red, combined HO₂ and O-species in purple, H₂O₂ in orange, OH recombination in yellow, three-body reactions (not covered above) in gray, and other reactions in black. The total rates of OH production and consumption are indicated for each region.

it falls within the range of local maxima of OH densities in the He/H₂O case, serving as a key reference for evaluating the role of entrainment dynamics. The solid target used for these experiments was a 2.5 cm diameter fused silica disk, with the effluent directed at the center of the disk. The corresponding 2D CFD simulations for these conditions are shown in figure 13, along with flow visualization measurements using a tracer gas to validate the CFD simulations.

Figure 12 shows that the overall 2D distributions of OH densities are similar to those of the open effluent cases prior to

approaching the surface. When the helium effluent strikes the surface, a stagnation zone is produced, directing the flow laterally along the surface, which carries the OH with the flow (figure 13). These dynamics are difficult to discern for the effluent propagating into air onto the surface 8 mm from the nozzle as the OH density has significantly decayed by that distance. For the effluent flowing into nitrogen, the OH closely follows the simulated helium carrier gas flow distribution due to the long lifetime of OH in the N₂ atmosphere. For both target distances, the horizontal extent of OH is significantly greater in

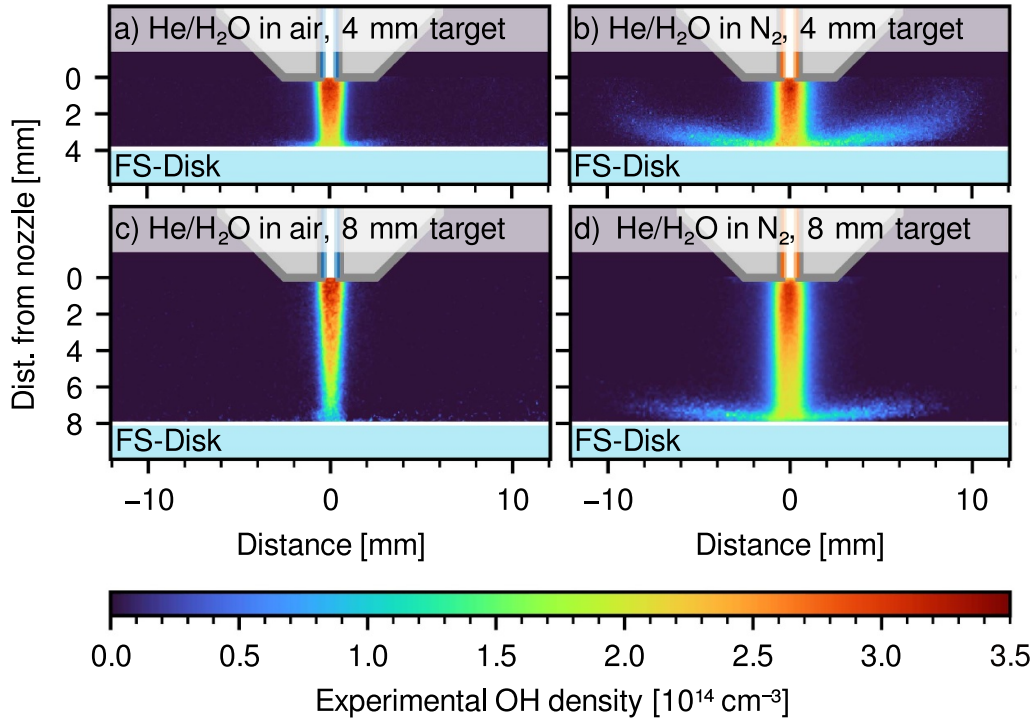


Figure 12. OH number density measurements for the effluent of a He/H₂O COST-Jet plasma in air and N₂ atmospheres impinging on solid targets at (a) and (b) 4 mm and (c) and (d) 8 mm from the jet's nozzle.

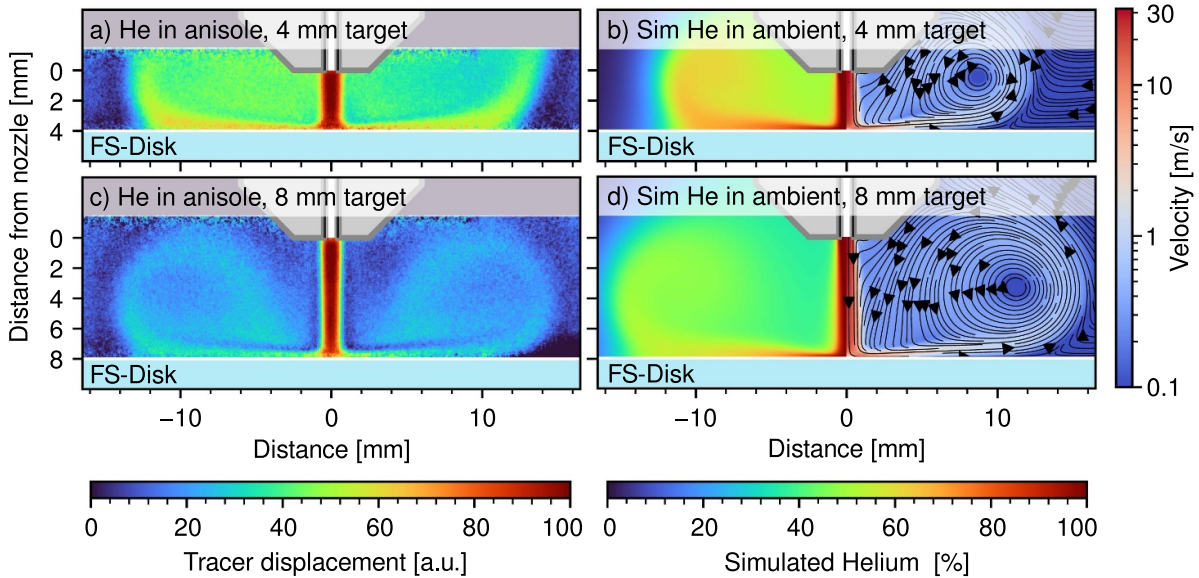


Figure 13. Anisole PLIF (no plasma) used as tracer gas to visualize the gas flow of He impinging on solid targets at two different distances (a) 4 mm and (c) 8 mm. Panels (b) and (d) are the 2D computed flow fields of the helium percent of the COST-Jet (without plasma) into ambient for each target case. The left side in panels (b) and (d) shows the simulated He mole fraction while the right side shows the flow velocity.

the N₂ atmosphere, reaching approximately five times further in the horizontal direction than it does in the air atmosphere. The measured distributions of OH dissipate more rapidly than the computed He percentages. We attribute this discrepancy to differences in the dimensionality of the experiment and simulation. The flow in the experiments is three-dimensional, with the flow at the nozzle being a 1 mm × 1 mm jet which has

mixing of the ambient gases into the effluent from all sides. With the CFD simulations being 2D, there is less mixing into the effluent and more vortexing of the flow.

The centerline profiles for OH number densities for both atmospheres, with and without targets, are plotted in figure 14 as a function of distance from the jet nozzle, in conjunction with the ambient gas percent extracted from the 2D fluid

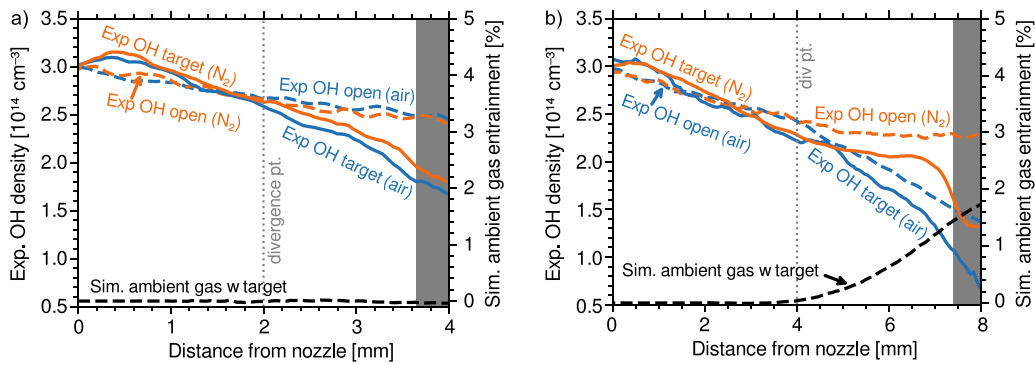


Figure 14. OH number density measurements on effluent centerline of a He/H₂O COST-Jet plasma, in air or N₂ atmosphere, as a function of distance from the jet nozzle, impinging on a solid target located (a) 4 mm or (b) 8 mm from the nozzle. Data are from corresponding images in figure 12. The black dashed lines correspond to the centerline profiles of the ambient gas percent from the CFD simulation with solid targets, as seen in figures 13(b) and (d). The OH centerline profiles for the He/H₂O case without a target, seen in figure 4, are also plotted here as dashed lines for comparison.

simulations. The gray rectangles in the plots indicate regions very close to the interface where measurement uncertainties are increased due to the boundary of the vignetting correction, which is less than 60 μm for both target cases. The OH density decreases linearly up to 4 mm for both target distances, with a slightly more rapid decline compared to the OH density observed in open ambient flow, which is similar to trends reported in [36] for a liquid target. This more rapid decrease is likely due to recirculation and vortexing of the He and entrained ambient gases which more rapidly mix the ambient with the He effluent. Additionally, the divergence point of OH densities between different atmospheres varies: at an 8 mm target distance, the divergence occurs at 4 mm, similar to the open effluent case. Conversely, when the target is positioned 4 mm from the jet nozzle, the centerline OH profiles diverge at 2 mm. This indicates that the atmosphere has a greater impact on OH densities and distribution when the effluent impinges on a target located 4 mm or closer to the jet nozzle.

4. Conclusions

PLIF was used to study the number density and spatial distribution of OH in the effluent of the COST atmospheric pressure plasma jet in the gas admixtures He/H₂O (0.25%) and He/O₂ (0.6%), propagating into N₂ and air atmospheres. To obtain absolute densities of OH, the spatial distribution of collisional quenching rates was measured directly for each gas mixture in each atmosphere, the laser beam profile was corrected by performing PLIF measurements of acetone or anisole, and a known amount of OH was generated by H₂O₂ photofragmentation to calibrate the signal.

The highest density of OH in the effluent occurred in the He/H₂O gas mixture, as OH is predominantly produced in the plasma by dissociation of water. The maximum density was $3 \times 10^{14} \text{ cm}^{-3}$ at the center of the nozzle exit. The gas mixture where no water is added, He/O₂, shows distinctly different density distributions. Here, the maximum OH density, $3.5 \times 10^{13} \text{ cm}^{-3}$, occurs at the edges of the nozzle and of the

effluent. The initial OH distribution results from ROS being produced dominantly at the sheath edge by electron impact dissociation of the O₂. The subsequent increase in OH densities occurs where these mix with the surrounding atmosphere. This leads to the formation of ‘reaction fronts’ as the ROS in the effluent are reacting with the surrounding (humid) atmospheres. The density in the center of the effluent is the same in nitrogen and air atmospheres for the first 4 mm from the nozzle. This downstream position coincides with the location where the ambient entrainment starts to reach the center of the effluent. Decreases in OH densities at further distances result from reactions with the ambient that consume the OH, whereas increases in OH densities results from reactions with the ambient that produce OH.

The OH densities for the He/H₂O gas mixture have distinct differences between the propagation in air and N₂ atmospheres. In N₂ atmosphere, the OH persists significantly farther downstream and is readily detected 30 mm from the nozzle exit, where the OH density in air atmosphere is approaching the detection limit at this distance. In the air atmosphere, the major OH consumption pathway is through HO₂ which can be created more efficiently when O₂ is present. In He/O₂, water is only present as an impurity in the discharge and as humidity in the surrounding atmosphere. Hence, lower OH densities were observed in the center of the effluent and higher density in the reaction fronts’ at the edge of the effluent. OH persists further in the effluent propagating into N₂, but the differences are not as stark as observed for He/H₂O mixtures.

By combining results from the 2D fluid simulation with a 0D global chemistry model, a pseudo 1-D simulation was used to investigate the reaction pathways of OH. In both cases, HO₂ was one of the dominant species involved in OH production in the effluent. H and O₂ are formed within the effluent for the He/H₂O mixture and as a result of mixing with the surrounding atmosphere for the He/O₂ mixture. HO₂ provides several pathways for OH production and consumption (He/H₂O). The major consumption pathway for OH in the He/O₂ mixture is the reaction with O, independent of the ambient atmosphere.

The effects of the COST-jet impinging on a solid target surface were investigated for two different target distances. The position of 4 mm from the nozzle was chosen because it is the divergence point for OH density in the center of the effluent when propagating into different atmospheres. For comparison, OH densities were measured for a solid surface at 8 mm. Both distances have been used as common treatment distances studied previously (e.g. [37, 40, 44]), therefore, these results could help contextualize other experiments. Meticulous accounting for vignetting, scattering, and other challenges of imaging near interfaces enabled OH densities to be determined with confidence as close as 60 μm to the interface. The OH densities on the centerline of the effluent impinging on the solid surface generally decreased more rapidly with distance than propagation into the open ambient. This more rapid decrease is likely due to recirculation and vortexing of the He effluent with the ambient which increases mixing of the ambient into the effluent.

Data availability statement

The data that support the findings of this study are contained within the article (and any supplementary files) and are available from the corresponding author upon reasonable request.

Acknowledgment

This work is based partly upon work supported by the U.S. Department of Energy, Office of Science, Office of Fusion Energy Sciences Opportunities in Frontier Plasma Science program under Award Number DE-SC-0021329.

The work of J Polito and M J Kushner was supported by the US National Science Foundation (CBET-2032604), and the US Department of Energy Office of Fusion Energy Sciences (DE-SC-0020232).

This research used resources of the Low Temperature Plasma Research Facility at Sandia National Laboratories, which is a collaborative research facility supported by the U.S. Department of Energy, Office of Science, Office of Fusion Energy Sciences.

Sandia National Laboratories is a multitechnology laboratory managed and operated by National Technology & Engineering Solutions of Sandia, LLC, a wholly owned subsidiary of Honeywell International Inc. for the U.S. Department of Energy's National Nuclear Security Administration under Contract DE-NA0003525. This paper describes objective technical results and analysis. Any subjective views or opinions that might be expressed in the paper do not necessarily represent the views of the DOE or the U.S. Government. The publisher acknowledges that the U.S. Government retains a non-exclusive, paid-up, irrevocable, world-wide license to publish or reproduce the published form of this written work or allow others to do so, for U.S. Government purposes. The DOE will provide public access to results of federally sponsored research in accordance with the DOE Public Access Plan.

This material is partly based upon work supported by the National Science Foundation under Grant No. PHY 2308857.

ORCID iDs

María J Herrera Quesada  <https://orcid.org/0000-0002-8623-550X>
 Sebastian Pfaff  <https://orcid.org/0000-0002-8528-9362>
 Grayson Gall  <https://orcid.org/0000-0003-0920-9719>
 Mark J Kushner  <https://orcid.org/0000-0001-7437-8573>
 Katharina Stapelmann  <https://orcid.org/0000-0002-2116-2661>

References

- [1] Bruggeman P and Leys C 2009 Non-thermal plasmas in and in contact with liquids *J. Phys. D: Appl. Phys.* **42** 053001
- [2] Gogate P R and Pandit A B 2004 A review of imperative technologies for wastewater treatment I: oxidation technologies at ambient conditions *Adv. Environ. Res.* **8** 501–51
- [3] Privat-Maldonado A, Schmidt A, Lin A, Weltmann K-D, Wende K, Bogaerts A and Bekeschus S 2019 ROS from physical plasmas: redox chemistry for biomedical therapy *Oxid. Med. Cell. Longev.* **2019** 9062098
- [4] Du H, Komuro A, Seki Y, Kobayashi M and Ono R 2024 Mechanism behind polypropylene surface modifications by OH radicals: an experimental study *Appl. Surf. Sci.* **648** 159086
- [5] Nakamura A, Shigemori S, Shimizu Y, Aoki T and Temmyo J 2004 Hydroxyl-radical-assisted growth of ZnO films by remote plasma metal-organic chemical vapor deposition *Jpn. J. Appl. Phys.* **43** 7672
- [6] Sabri M M, Jung J, Yoon D H, Yoon S, Tak Y J and Kim H J 2015 Hydroxyl radical-assisted decomposition and oxidation in solution-processed indium oxide thin-film transistors *J. Mater. Chem. C* **3** 7499–505
- [7] Golda J et al 2016 Concepts and characteristics of the cost reference microplasma jet *J. Phys. D: Appl. Phys.* **49** 084003
- [8] Benedikt J, Schröder D, Schneider S, Willems G, Pajdarová A, Vlček J and Schulz-von der Gathen V 2016 Absolute OH and O radical densities in effluent of a He/H₂O micro-scaled atmospheric pressure plasma jet *Plasma Sources Sci. Technol.* **25** 045013
- [9] Schröter S et al 2018 Chemical kinetics in an atmospheric pressure helium plasma containing humidity *Phys. Chem. Chem. Phys.* **20** 24263–86
- [10] Verreycken T, Mensink R, Van Der Horst R, Sadeghi N and Bruggeman P J 2013 Absolute OH density measurements in the effluent of a cold atmospheric-pressure Ar–H₂O RF plasma jet in air *Plasma Sources Sci. Technol.* **22** 055014
- [11] Voráč J, Dvořák P, Procházka V, Ehlbeck J and Reuter S 2013 Measurement of hydroxyl radical (OH) concentration in an argon RF plasma jet by laser-induced fluorescence *Plasma Sour. Sci. Technol.* **22** 025016
- [12] Ono R and Oda T 2008 Measurement of gas temperature and OH density in the afterglow of pulsed positive corona discharge *J. Phys. D: Appl. Phys.* **41** 035204
- [13] Dilecce G and De Benedictis S 2011 Laser diagnostics of high-pressure discharges: laser induced fluorescence detection of OH in He/Ar–H₂O dielectric barrier discharges *Plasma Phys. Control. Fusion* **53** 124006
- [14] Verreycken T, Sadeghi N and Bruggeman P 2014 Time-resolved absolute OH density of a nanosecond pulsed discharge in atmospheric pressure He–H₂O: absolute calibration, collisional quenching and the importance of

- charged species in OH production *Plasma Sources Sci. Technol.* **23** 045005
- [15] Reuter S, Sousa J S, Stancu G D and Hubertus van Helden J-P 2015 Review on VUV to MIR absorption spectroscopy of atmospheric pressure plasma jets *Plasma Sources Sci. Technol.* **24** 054001
- [16] Budde M, Martini L M, Ceppelli M, Quercetti S and Engeln R 2022 Absolute OH density measurements in a CO₂-H₂O glow discharge by laser-induced fluorescence spectroscopy *Plasma Sources Sci. Technol.* **31** 055002
- [17] van den Bekerom D, Tahiyat M M, Huang E, Frank J H and Farouk T I 2023 2D-imaging of absolute OH and H₂O₂ profiles in a He-H₂O nanosecond pulsed dielectric barrier discharge by photo-fragmentation laser-induced fluorescence *Plasma Sources Sci. Technol.* **32** 015006
- [18] Aldén M, Edner H, Holmstedt G, Svanberg S and Högberg T 1982 Single-pulse laser-induced OH fluorescence in an atmospheric flame, spatially resolved with a diode array detector *Appl. Opt.* **21** 1236-40
- [19] Faust S, Dreier T and Schulz C 2013 Photo-physical properties of anisole: temperature, pressure and bath gas composition dependence of fluorescence spectra and lifetimes *Appl. Phys. B* **112** 203-13
- [20] Holt R, McLane C and Oldenberg O 1948 Erratum: ultraviolet absorption spectrum of hydrogen peroxide *J. Chem. Phys.* **16** 638-638
- [21] Vaghjiani G L, Turnipseed A A, Warren R F and Ravishankara A 1992 Photodissociation of H₂O₂ at 193 and 222 nm: products and quantum yields *J. Chem. Phys.* **96** 5878-86
- [22] Gaston D, Newman C, Hansen G and Lebrun-Grandie D 2009 MOOSE: a parallel computational framework for coupled systems of nonlinear equations *Nucl. Eng. Des.* **239** 1768-78
- [23] Peterson J W, Lindsay A D and Kong F 2018 Overview of the incompressible Navier-Stokes simulation capabilities in the MOOSE framework *Adv. Eng. Softw.* **119** 68-92
- [24] Geuzaine C and Remacle J-F 2009 Gmsh: a 3-D finite element mesh generator with built-in pre- and post-processing facilities *Int. J. Numer. Methods Eng.* **79** 1309-31
- [25] Lin P, Zhang J, Nguyen T, Donnelly V M and Economou D J 2020 Numerical simulation of an atmospheric pressure plasma jet with coaxial shielding gas *J. Phys. D: Appl. Phys.* **54** 075205
- [26] Engineeringtoolbox Editor 2023 Helium - density and specific weight vs. temperature and pressure (available at: www.engineeringtoolbox.com/helium-density-specific-weight-temperature-pressure-d_2090.html)
- [27] Engineeringtoolbox Editor 2023 Gases - dynamic viscosities (available at: www.engineeringtoolbox.com/gases-absolute-dynamic-viscosity-d_1888.html)
- [28] Wasik S and McCulloh K 1969 Measurements of gaseous diffusion coefficients by a gas chromatographic technique *J. Res. Natl Bureau Stand. A* **73** 207
- [29] Engineeringtoolbox Editor 2023 Nitrogen - density and specific weight vs. temperature and pressure (available at: www.engineeringtoolbox.com/nitrogen-N2-density-specific-weight-temperature-pressure-d_2039.html)
- [30] Engineeringtoolbox Editor 2023 Oxygen - density and specific weight vs. temperature and pressure (available at: www.engineeringtoolbox.com/oxygen-O2-density-specific-weight-temperature-pressure-d_2082.html)
- [31] Lietz A M and Kushner M J 2016 Air plasma treatment of liquid covered tissue: long timescale chemistry *J. Phys. D: Appl. Phys.* **49** 425204
- [32] Kruszelnicki J, Lietz A and Kushner M 2019 Atmospheric pressure plasma activation of water droplets *J. Phys. D: Appl. Phys.* **52** 355207
- [33] Polito J and Kushner M J 2024 A hierarchical model for bacterial cell inactivation in solution by direct and indirect treatment using cold atmospheric plasmas *J. Phys. D: Appl. Phys.* **57** 405207
- [34] Baulch D, Cox R, Hampson R F, Kerr J, Troe J and Watson R 1980 Evaluated kinetic and photochemical data for atmospheric chemistry *J. Phys. Chem. Ref. Data* **9** 295-472
- [35] Baulch D, Cox R, Crutzen P, Hampson R, Kerr J, Troe J and Watson R T 1982 Evaluated Kinetic and photochemical data for atmospheric chemistry: supplement I CODATA task group on chemical kinetics *J. Phys. Chem. Ref. Data* **11** 327-496
- [36] Stapelmann K, Myers B, Quesada M H, Lenker E and Ranieri P J 2021 Following O and OH in He/O₂ and He/H₂O gas mixtures-From the gas phase through the liquid phase to modifications on a biological sample *J. Phys. D: Appl. Phys.* **54** 434003
- [37] Myers B, Ranieri P, Smirnova T, Hewitt P, Peterson D, Quesada M H, Lenker E and Stapelmann K 2021 Measuring plasma-generated OH and O atoms in liquid using EPR spectroscopy and the non-selectivity of the HTA assay *J. Phys. D: Appl. Phys.* **54** 145202
- [38] Schneider S, Dünnebier M, Hübner S, Reuter S and Benedikt J 2014 Atomic nitrogen: a parameter study of a micro-scale atmospheric pressure plasma jet by means of molecular beam mass spectrometry *J. Phys. D: Appl. Phys.* **47** 505203
- [39] Polito J, Quesada M J H, Stapelmann K and Kushner M J 2023 Reaction mechanism for atmospheric pressure plasma treatment of cysteine in solution *J. Phys. D: Appl. Phys.* **56** 395205
- [40] Wapshott-Stehli H L, Myers B G, Herrera Quesada M J, Grunden A and Stapelmann K 2022 Plasma-driven biocatalysis: in situ hydrogen peroxide production with an atmospheric pressure plasma jet increases the performance of OleTJE when compared to adding the same molar amount of hydrogen peroxide in bolus *Plasma Process. Polym.* **19** 2100160
- [41] Ranieri P, Mohamed H, Myers B, Dobossy L, Beyries K, Trosan D, Krebs F C, Miller V and Stapelmann K 2020 GSH modification as a marker for plasma source and biological response comparison to plasma treatment *Appl. Sci.* **10** 2025
- [42] Lackmann J-W et al 2018 Chemical fingerprints of cold physical plasmas—an experimental and computational study using cysteine as tracer compound *Sci. Rep.* **8** 7736
- [43] Riedel F, Golda J, Held J, Davies H, van der Woude M, Bredin J, Niemi K, Gans T, Schulz-von der Gathen V and O'Connell D 2020 Reproducibility of COST reference microplasma jets *Plasma Sources Sci. Technol.* **29** 095018
- [44] Benedikt J, Hefny M M, Shaw A, Buckley B R, Iza F, Schäfermann S and Bandow J E 2018 The fate of plasma-generated oxygen atoms in aqueous solutions: non-equilibrium atmospheric pressure plasmas as an efficient source of atomic O (AQ) *Phys. Chem. Chem. Phys.* **20** 12037-42